We are IntechOpen,
the world's leading publisher of Open Access books
Built by scientists, for scientists

6,900
Open access books available

186,000
International authors and editors

200M
Downloads

154
Countries delivered to

Our authors are among the

TOP 1%
most cited scientists

12.2%
Contributors from top 500 universities

CLARIVATE ANALYTICS
BOOK CITATION INDEX
INDEXED

WEB OF SCIENCE™

Selection of our books indexed in the Book Citation Index
in Web of Science™ Core Collection (BKCI)

Interested in publishing with us?
Contact book.department@intechopen.com

Layered Cobaltites and Natural Chalcogenides for Thermoelectrics

Ran Ang

Additional information is available at the end of the chapter

Abstract

We have systematically investigated thermoelectric properties by a series of doping in layered cobaltites $Bi_2Sr_2Co_2O_y$, verifying the contribution of narrow band. In particular, Sommerfeld coefficient is dependent on charge carriers' density and as function of density of states (DOS) at Fermi level, which is responsible for the persistent enhancement of large thermoelectric power. Especially for $Bi_2Sr_{1.9}Ca_{0.1}Co_2O_y$, it may provide an excellent platform to be a promising candidate of thermoelectric materials. On the other hand, high-performance thermoelectric materials require elaborate doping and synthesis procedures, particularly the essential thermoelectric mechanism still remains extremely challenging to resolve. In this chapter, we show evidence that thermoelectricity can be directly generated by a natural chalcopyrite mineral $Cu_{1+x}Fe_{1-x}S_2$ from a deep-sea hydrothermal vent, wherein the resistivity displays an excellent semiconducting character, while the large thermoelectric power and high power factor emerge in the low x region where the electron-magnon scattering and large effective mass manifest, indicative of the strong coupling between doped carriers and localized antiferromagnetic spins, adding a new dimension to realizing the charge dynamics. The present findings advance our understanding of basic behaviors of exotic states and demonstrate that low-cost thermoelectric energy generation and electron/hole carrier modulation in naturally abundant materials is feasible.

Keywords: layered cobalt oxides, narrow band contribution, natural chalcopyrite mineral, thermoelectricity generation, electron-magnon scattering

1. Introduction

Layered cobaltites with CdI_2-type CoO_2 block provide an excellent platform for investigating thermoelectric properties. A key to unveil mysterious thermoelectric properties lies in the two-dimensional (2D) conducting CoO_2 layer. For layered Bi-A-Co-O (A = Ca, Sr, and Ba), it also contains analogous conducting CoO_2 layer [1]. In particular, layered $Bi_2Sr_2Co_2O_y$ (BSC)

exhibits a rather large thermoelectric power S ($\sim$100 µV/K) at room temperature, which makes $Bi_2Sr_2Co_2O_y$ one of promising thermoelectric materials from the viewpoint of potential applications, analogous to other misfit-layered cobaltites, such as $NaCo_2O_4$ and $Ca_3Co_4O_9$ [2–5]. However, most studies of $Bi_2Sr_2Co_2O_y$ system are mainly focused on the thermoelectric improvement [2, 3, 6]. The transport mechanism based on resistivity ρ and thermoelectric power S has not been clarified. Moreover, large S is totally different from conventional value (<10 µV/K) based on a broad band model [7]. In this chapter, we will show evidence on a narrow band contribution in doped $Bi_2Sr_2Co_2O_y$ [8]. And what's more, exotic enhancement of large S is related to local density of states (DOS) near Fermi level (E_F) [9]. It could be effectively modulated thermoelectric performance by utilizing different doping. It is plausible to distinguish, which thermoelectric materials in doped $Bi_2Sr_2Co_2O_y$ could be regarded as potential candidates.

On the other hand, ternary chalcogenides serve as an ideal platform for investigating intricate physical and chemical characteristics controlling the efficiency of thermoelectric materials, and also are promising materials for potential applications in photovoltaics, luminescence, as well as thermoelectric and spintronic devices [10–13]. Ternary chalcopyrite-structured chalcogenides, such as $CuFeS_2$, have attracted particular attention owing to their unique optical, electrical, magnetic, and thermal properties [14–28]. Studies on chalcopyrite ($CuFeS_2$) have primarily focused on its electronic states [14, 15, 29–31]. However, the microscopic mechanism of electronic structure and thermoelectric character in $CuFeS_2$, which presumably arises from some scenarios such as delocalization of the Fe $3d$ electrons, charge-transfer-driven hybridization between Fe $3d$ and S $3p$ orbitals, or density of the conduction band electron states, still remains highly controversial [17, 30, 32]. The intrinsic mechanism of good thermoelectric properties is still a vital question which needs to be clarified. Another important issue is that the fabrication of artificial chalcopyrite itself requires expensively complex synthesis procedures and relatively high cost of constituent precursors, thereby potentially limiting the large-scale applications in the thermoelectric field.

In this chapter, we confirm that an unexpected thermoelectricity can directly be generated in a natural chalcopyrite mineral $Cu_{1+x}Fe_{1-x}S_2$ from a deep-sea hydrothermal vent, and demonstrate that doped carriers have strong coupling with localized antiferromagnetic (AFM) spins, which greatly enhance the thermoelectric power S and power factor, revealing the significance of electron-magnon scattering and large effective mass [33]. This will open up another useful avenue in manipulating low-cost thermoelectricity or even electron/hole carriers via the natural energy materials abundantly deposited in the earth.

2. Thermoelectric properties and narrow band contribution of $Bi_2Sr_{1.9}M_{0.1}Co_2O_y$ and $Bi_2Sr_2Co_{1.9}X_{0.1}O_y$

2.1. Crystal structure and valence states of Co ions

The crystal structure of $Bi_2Sr_2Co_2O_y$ is shown in the inset in **Figure 1**, where conducting CoO_2 layer with triangular lattice and insulating rocksalt $Bi_2Sr_2O_4$ block layer are alternatively stacked along c-axis, similar to the case of high-temperature superconductors like $Bi_2Sr_2CaCu_2O_y$.

Scanning electron microscopy (SEM) characterization of $Bi_2Sr_2Co_2O_y$ indicates surface morphology of plate-like grains. **Figure 1** shows X-ray diffraction (XRD) patterns of selected samples $Bi_2Sr_2Co_2O_y$, $Bi_2Sr_{1.9}Ca_{0.1}Co_2O_y$, and $Bi_2Sr_2Co_{1.9}Mo_{0.1}O_y$ with single phase, in agreement with XRD result of $Bi_{1.4}Pb_{0.6}Sr_2Co_2O_y$ [34]. The average Co valence was determined based on energy dispersive spectroscopy (EDS) measurement for all samples. For $Bi_2Sr_2Co_2O_y$, average Co valence is +3.330. For $Bi_2Sr_{1.9}M_{0.1}Co_2O_y$ (M = Ag, Ca, and Y), average Co valence is +3.380, +3.330, and +3.280, respectively. For $Bi_2Sr_2Co_{1.9}X_{0.1}O_y$ (X = Zr, Al, and Mo), average Co valence is +3.295, +3.347, and +3.189, respectively. X-ray photoemission spectroscopy (XPS) spectra (see **Figure 4a**) also show the valence states of Co $2p_{3/2}$ and $2p_{1/2}$ for selected $Bi_2Sr_{1.9}Ca_{0.1}Co_2O_y$ sample. Photon energy of Co $2p_{3/2}$ and $2p_{1/2}$ is 779.4 and 794.2 eV, respectively, demonstrating mixed Co valence between +3 and +4.
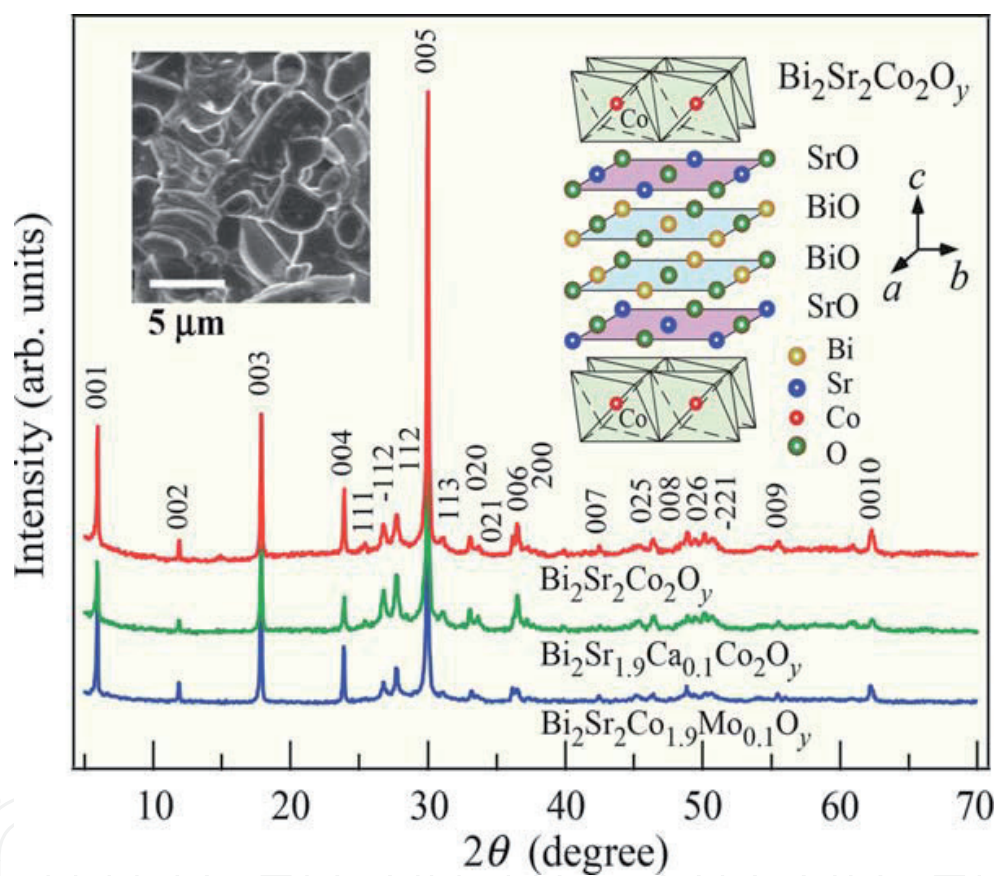

Figure 1. Powder XRD patterns for $Bi_2Sr_2Co_2O_y$, $Bi_2Sr_{1.9}Ca_{0.1}Co_2O_y$, and $Bi_2Sr_2Co_{1.9}Mo_{0.1}O_y$ samples at room temperature. Inset: crystal structure and SEM image of $Bi_2Sr_2Co_2O_y$.

2.2. Resistivity and transport mechanism

Figure 2a and **d** shows temperature dependence of resistivity $\rho(T)$ of all samples. For parent $Bi_2Sr_2Co_2O_y$ sample, an upturning point at T_p (~75 K) is observed. Metallic behavior above T_p appears, demonstrating existence of itinerant charge carriers. Compared with $Bi_2Sr_2Co_2O_y$, $\rho(T)$ of all doped samples (except $Bi_2Sr_{1.9}Ca_{0.1}Co_2O_y$) display total increase in view of the disorder effect. Furthermore, enhanced random Coulomb potential because of the doping induces the obvious shift of T_p toward higher temperature. On the other hand, $\rho(T)$ of $Bi_2Sr_{1.9}Ca_{0.1}Co_2O_y$ presents an overall decrease due to introduction of hole–type charge carriers into conducting CoO_2 layers.
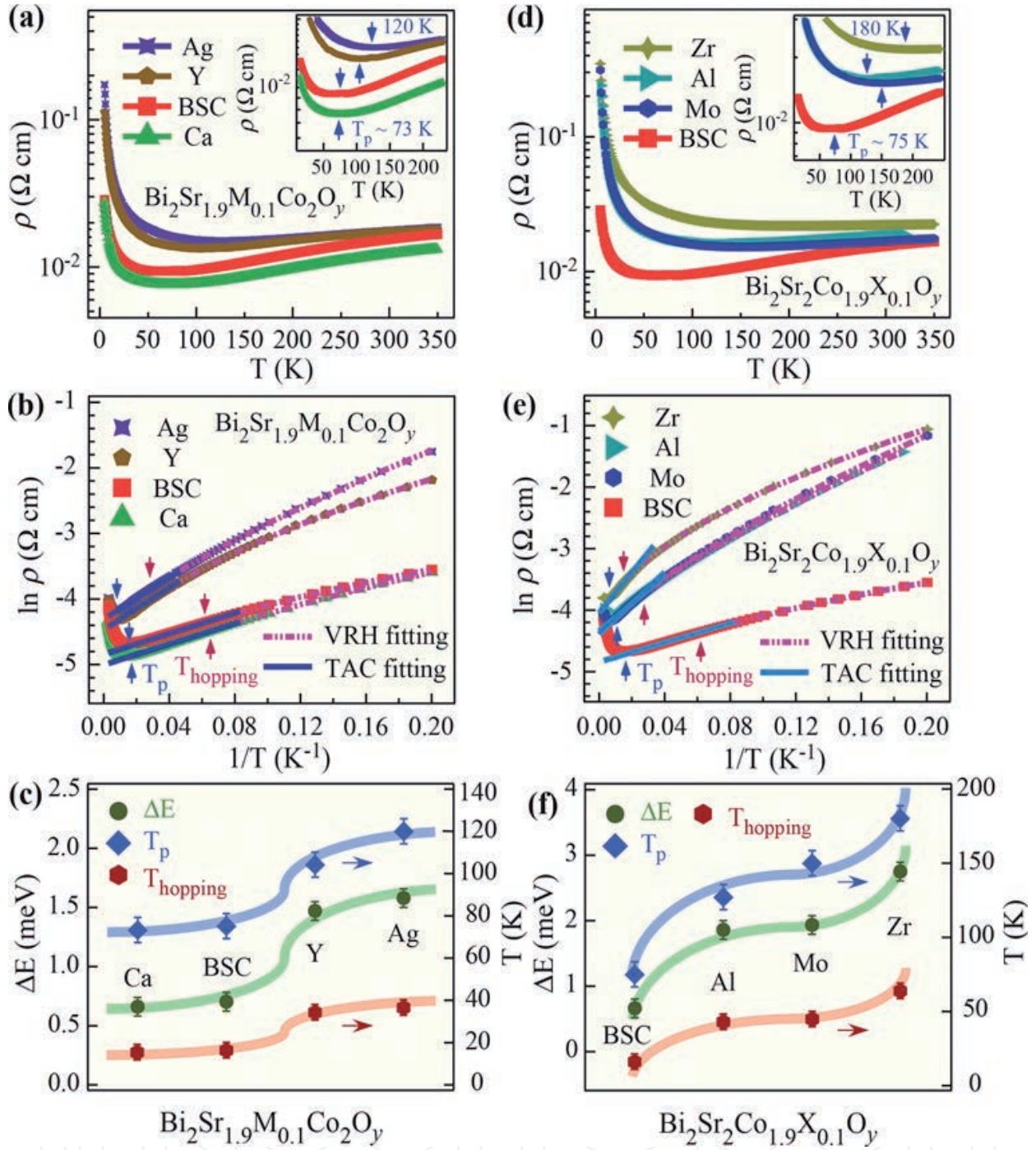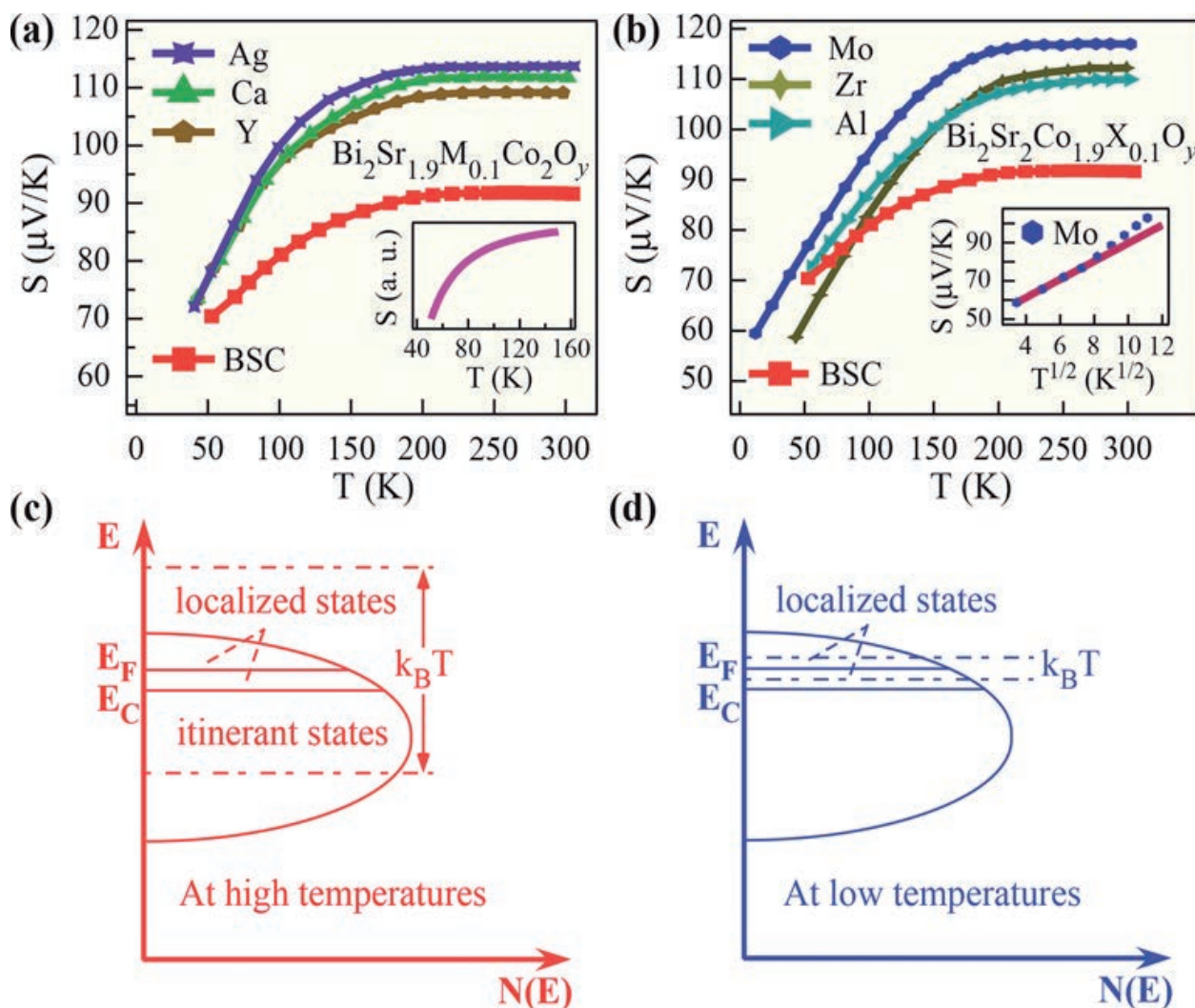
Figure 2. (a) Temperature dependence of resistivity $\rho(T)$ and inset: magnification plot of $\rho(T)$ for $Bi_2Sr_2Co_2O_y$ (BSC) and $Bi_2Sr_{1.9}M_{0.1}Co_2O_y$ (M = Ag, Ca, and Y) samples. (b) Plot of $\ln \rho$ against T^{-1} for $Bi_2Sr_2Co_2O_y$ and $Bi_2Sr_{1.9}M_{0.1}Co_2O_y$ samples. Solid lines stand for TAC fitting. Dashed curves express VRH fitting. (c) $Bi_2Sr_2Co_2O_y$ and $Bi_2Sr_{1.9}M_{0.1}Co_2O_y$ dependence of activation energy ΔE, onset temperature T_p of TAC, and onset temperature $T_{hopping}$ of VRH. The shadow in bold is guide to the eyes. (d)–(f) are similar to (a)–(c) but for $Bi_2Sr_2Co_{1.9}X_{0.1}O_y$ (X = Zr, Al, and Mo) samples.

To get insight into the conduction mechanism below T_p, dependences of $\ln \rho$ on T^{-1} are plotted in **Figure 2b** and **e**. At the beginning, it is found that thermally activated conduction (TAC) law matches $\rho(T)$ data well below T_p, namely [35], $\rho(T) = \rho_0 \exp(\Delta E/k_B T)$, where ΔE is activation energy. Interestingly, $\rho(T)$ apparently deviates from the TAC behavior with decreasing temperature further, and it follows Mott's variable-range-hopping (VRH) model described by equation

[35]: $\rho(T) = \rho_0 \exp[(T_0/T)^n]$. As seen from **Figure 2c** and **f**, obtained values of ΔE and onset temperature T_{hopping} of $Bi_2Sr_{1.9}Ca_{0.1}Co_2O_y$ (0.66 meV and 15.3 K) are the respective minimum, even smaller, than those of parent $Bi_2Sr_2Co_2O_y$ (0.70 meV and 16.2 K), while ΔE and T_{hopping} of $Bi_2Sr_2Co_{1.9}Zr_{0.1}O_y$ (2.75 meV and 63.6 K) are both maximum among all samples.

2.3. Thermoelectric power and narrow band model

Figure 3a and **b** shows temperature dependence of thermoelectric power $S(T)$ for all samples. Positive values of S reflect electrical transport feature dominated by holes. Values of S at room temperature for all doped samples produce a substantial increase, especially for $Bi_2Sr_2Co_{1.9}Mo_{0.1}O_y$ (~117 μV/K), compared with pristine $Bi_2Sr_2Co_2O_y$ (~92 μV/K). Particularly, with decreasing the temperature until below T_{hopping}, $S(T)$ behavior follows with VRH model [36]: $S_{\text{VRH}}(T) \sim aT^{1/2}$, where a is factor determined by density of localized states at Fermi level $N(E_F)$. The inset in **Figure 3b** reveals Anderson localization of $Bi_2Sr_2Co_{1.9}Mo_{0.1}O_y$, in correspondence with low-temperature resistivity.
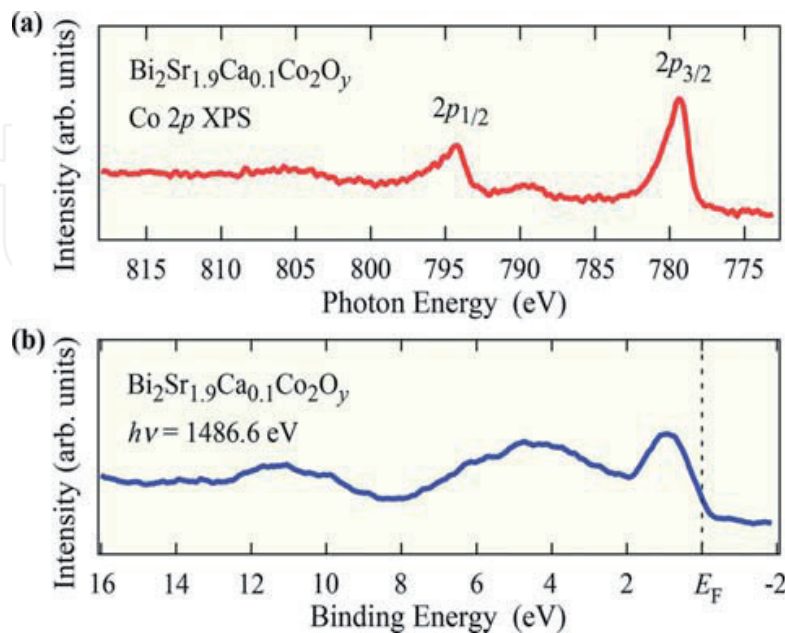

Figure 3. Temperature dependence of thermoelectric power $S(T)$ for $Bi_2Sr_2Co_2O_y$, (**a**) $Bi_2Sr_{1.9}M_{0.1}Co_2O_y$ (M = Ag, Ca, and Y), and (**b**) $Bi_2Sr_2Co_{1.9}X_{0.1}O_y$ (X = Zr, Al, and Mo) samples. Inset: calculated and fitted results of (**a**) Boltzmann formula and (**b**) VRH model for $Bi_2Sr_2Co_{1.9}Mo_{0.1}O_y$ sample, respectively. Schematic diagram of density of states in a narrow band with Anderson localization at (**c**) high temperatures (metallic or TAC region) and (**d**) low temperatures (VRH region).

In general, S is extremely small (<10 µV/K) and presents a metallic behavior in a broad band [7]. Taking into account the huge difference, large S at high temperatures (above 200 K) in a narrow band matches Heikes model [37]: $S = k_B/e\{\ln[d/(1-d)]\}$, where d is concentration of Co^{4+}. The enhanced S at high temperatures is attributed to the competition between d and spin entropy. It is noted that $S(T)$ is also described by narrow band model at intermediate temperatures. $S(T)$ follows with Boltzmann formula [38]: $S(T) = 1/eT\{\int(E-E_F)E^2dE/[e^{(E-E_F)/2k_BT} + e^{-(E-E_F)/2k_BT}]^2\}/\{\int E^2 dE/[e^{(E-E_F)/2k_BT} + e^{-(E-E_F)/2k_BT}]^2\}$. Calculated $S(T)$ indicates monotonous increase with increasing T, as well as experimental result as plotted in the inset in **Figure 3a**, revealing the validity of narrow band model.

Actually, activation energy ΔE is equal to E_F-E_C, where E_C is the upper mobility edge. As $k_BT/2 > \Delta E$, conduction mainly determined by contribution of excited holes in itinerant states as specified in **Figure 3c**. At high temperatures, the majority of acceptor-like states are fully ionized, that is, occurs complete excitation of holes, that resulting in metallic behavior of $\rho(T)$ and diffused $S(T)$ (Heikes formula). As $k_BT/2$ is near to ΔE, TAC conduction forms (Boltzmann dispersion). As $k_BT/2 < \Delta E$, VRH conduction dominates the transport mechanism as shown in **Figure 3d**.

### 2.4. X-ray photoemission spectroscopy and thermal conductivity

In order to further verify the narrow band model, we carried out XPS spectra for $Bi_2Sr_{1.9}Ca_{0.1}Co_2O_y$. As shown in **Figure 4b**, XPS spectra present an intense peak at ~ 0.95 eV, in line with large S and metallic behavior. Between E_F and ~2.0 eV, Co $3d$ and O $2p$ orbitals play an important role, similar to pristine $Bi_2Sr_2Co_2O_y$ [39]. Moreover, strong hybridization between Co $3d$ and O $2p$ forms [39, 40]. Namely, antibonding t_{2g} narrow bands contribute to intense peak at ~0.95 eV, while bonding e_g broad bands are responsible to peak within 3–8 eV. In addition, calculated $S(T)$ is also consistent with experimental value based on magnitude and temperature dependence [39]. Therefore, the narrow band model is very suitable for explaining all experimental and theoretical results.

Figure 4. (**a**) Co $2p$ XPS spectra and (**b**) XPS spectra in wide binding-energy range for selected $Bi_2Sr_{1.9}Ca_{0.1}Co_2O_y$ sample at room temperature.

Temperature dependence of total thermal conductivity $\kappa(T)$ for all samples are shown in **Figure 5a** and **d**. $\kappa(T)$ can be expressed by the sum of phononic component $\kappa_{ph}(T)$ and mobile charge carriers' component $\kappa_e(T)$ as $\kappa(T) = \kappa_{ph}(T) + \kappa_e(T)$. Value of $\kappa_e(T)$ can be estimated from the Wiedemann-Franz law, $\kappa_e(T) = L_0 T/\rho$, where $L_0 \sim 2.44 \times 10^{-8}$ V^2/K^2 stands for Lorenz number. In **Figure 5b** and **e**, $\kappa_{ph}(T)$ dominates the thermal conductivity because CoO$_2$ layer and Bi-Sr-O block layer induces the interface scattering. Dimension less figure of merit $ZT = S^2 T/\rho\kappa$ reflects total thermoelectric performance (see **Figure 5c** and **f**). For pristine Bi$_2$Sr$_2$Co$_2$O$_y$, ZT value reaches ~ 0.007 at 300 K, while ZT value reaches 0.19 at 973 K, indicative of promising thermoelectric material for Bi$_2$Sr$_2$Co$_2$O$_y$ at high temperatures [2]. Especially for Bi$_2$Sr$_{1.9}$Ca$_{0.1}$Co$_2$O$_y$, ZT value reaches maximum ~ 0.012 at 137 K. Therefore, it is reasonable to predict that Bi$_2$Sr$_{1.9}$Ca$_{0.1}$Co$_2$O$_y$ could be considered as one of potential ultra-high temperature thermoelectric materials, as well as pristine Bi$_2$Sr$_2$Co$_2$O$_y$.
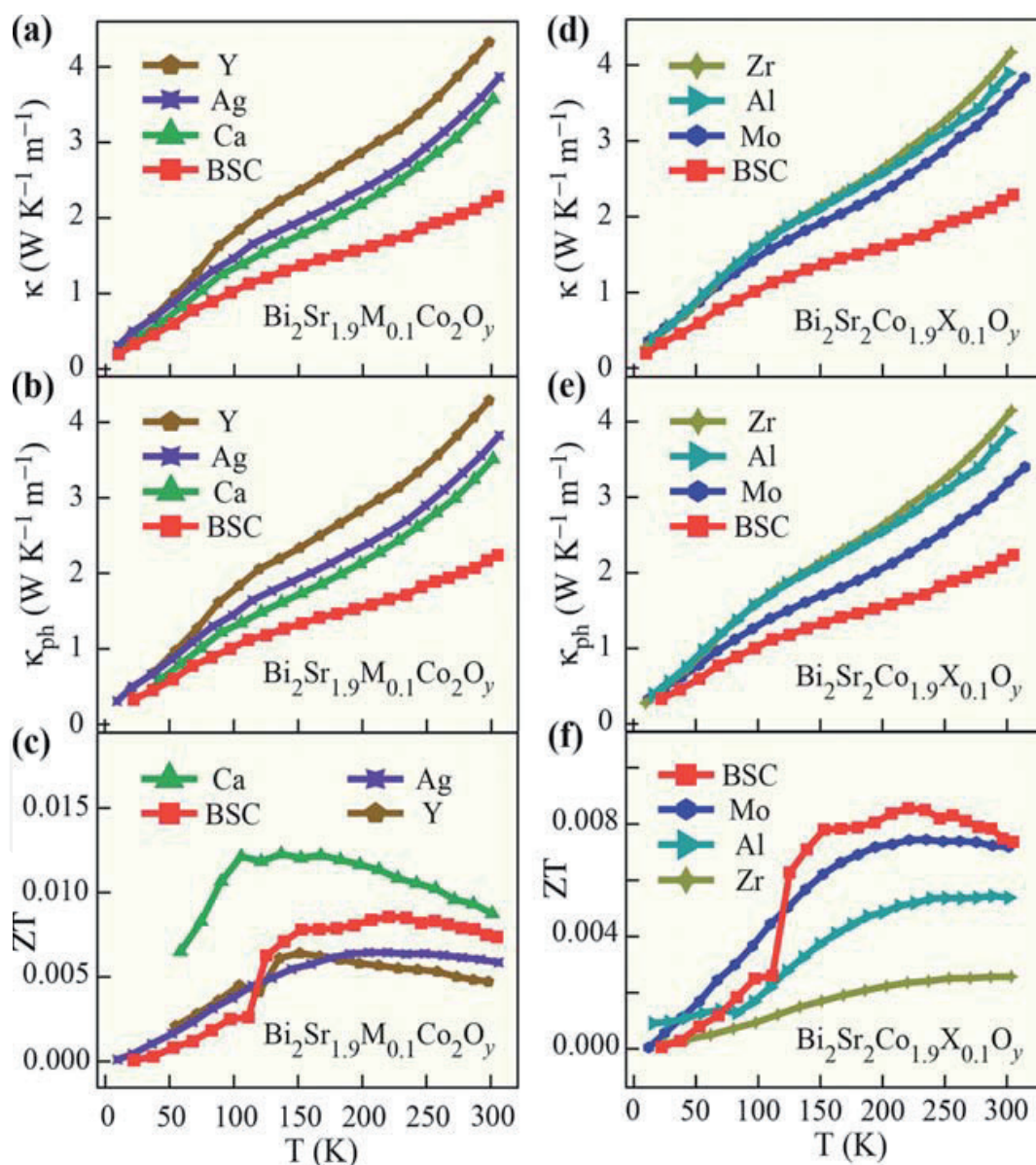

Figure 5. Temperature dependence of (**a**) total thermal conductivity $\kappa(T)$, (**b**) phononic component $\kappa_{ph}(T)$, and (**c**) dimensionless figure of merit ZT for BSC and Bi$_2$Sr$_{1.9}$M$_{0.1}$Co$_2$O$_y$ (M = Ag, Ca, and Y) samples. (**d**)–(**f**) are similar to (**a**)–(**c**), but for Bi$_2$Sr$_2$Co$_{1.9}$X$_{0.1}$O$_y$ (X = Zr, Al, and Mo) samples.

3. Exotic reinforcement of thermoelectric power in layered Bi$_2$Sr$_{2-x}$Ca$_x$Co$_2$O$_y$

3.1. XRD patterns and electrical transport properties

The crystal structure of Bi$_2$Sr$_2$Co$_2$O$_y$ is shown in **Figure 6a**. **Figure 6b** shows XRD patterns of all Ca-doping samples with single phase in Bi$_2$Sr$_{2-x}$Ca$_x$Co$_2$O$_y$ ($0.0 \leq x \leq 2.0$). With increasing Ca content, diffraction peak along [003] direction distinctly shifts to higher angle as shown in the inset in **Figure 6b**, confirming the smaller ionic radius of Ca^{2+}, than that of Sr^{2+}. SEM characterization indicates surface morphology of plate-like grains and regular grain sizes for selected samples with $x = 0.0$ and 1.0, respectively.
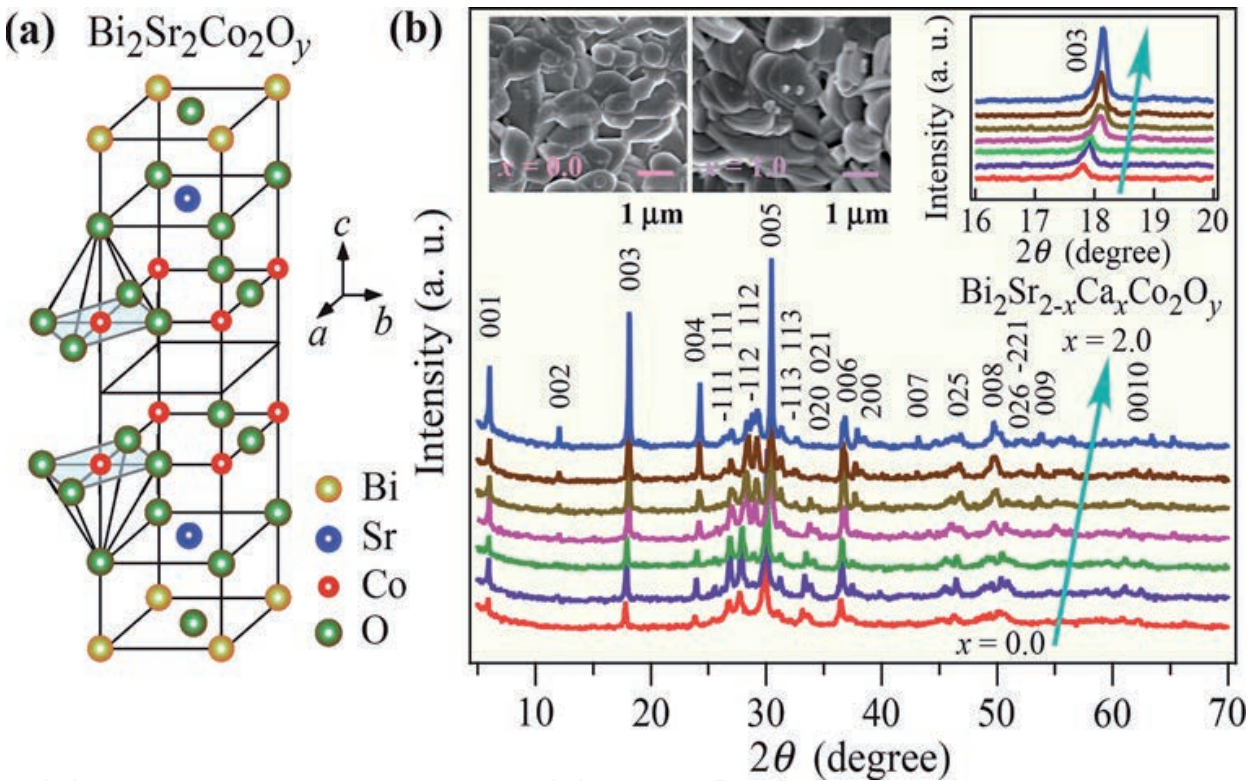
Figure 6. (**a**) Crystal structure of Bi$_2$Sr$_2$Co$_2$O$_y$. (**b**) Powder XRD patterns for Bi$_2$Sr$_{2-x}$Ca$_x$Co$_2$O$_y$ ($0.0 \leq x \leq 2.0$) samples at room temperature. Insets: magnified powder's XRD patterns along [003] direction for all samples and SEM images for selected samples with $x = 0.0$ and 1.0, respectively.

Figure 7a and **b** shows resistivity $\rho(T)$ of all samples in Bi$_2$Sr$_{2-x}$Ca$_x$Co$_2$O$_y$. For the present $x = 0.0$ polycrystalline sample, upturning point at T_p (~150 K) appears. Metallic behavior above T_p is observed, demonstrating the existence of itinerant charge carriers. In comparison, for $x = 0.0$ single crystal [41], in-plane resistivity ρ_{ab} also shows metallic behavior around room temperature, while it arises minimum near 80 K and diverges with further decreasing the temperature. Resistivity ρ_{ab} value of single crystal for $x = 0.0$ at room temperature is ~4 mOhm×cm and is smaller than that of our polycrystalline sample (~15 mOhm×cm). On the other hand, compared with $x = 0.0$, $\rho(T)$ of all Ca-doped samples produce total increase due to disorder effect. For the samples with $x \leq 0.5$, enhanced random Coulomb potential because of Ca doping induces the shift of T_p toward higher temperature. Interestingly, for the samples

with $x \geq 1.0$, the signature of transition at T_p completely vanishes and $\rho(T)$ only presents an insulating-like behavior.
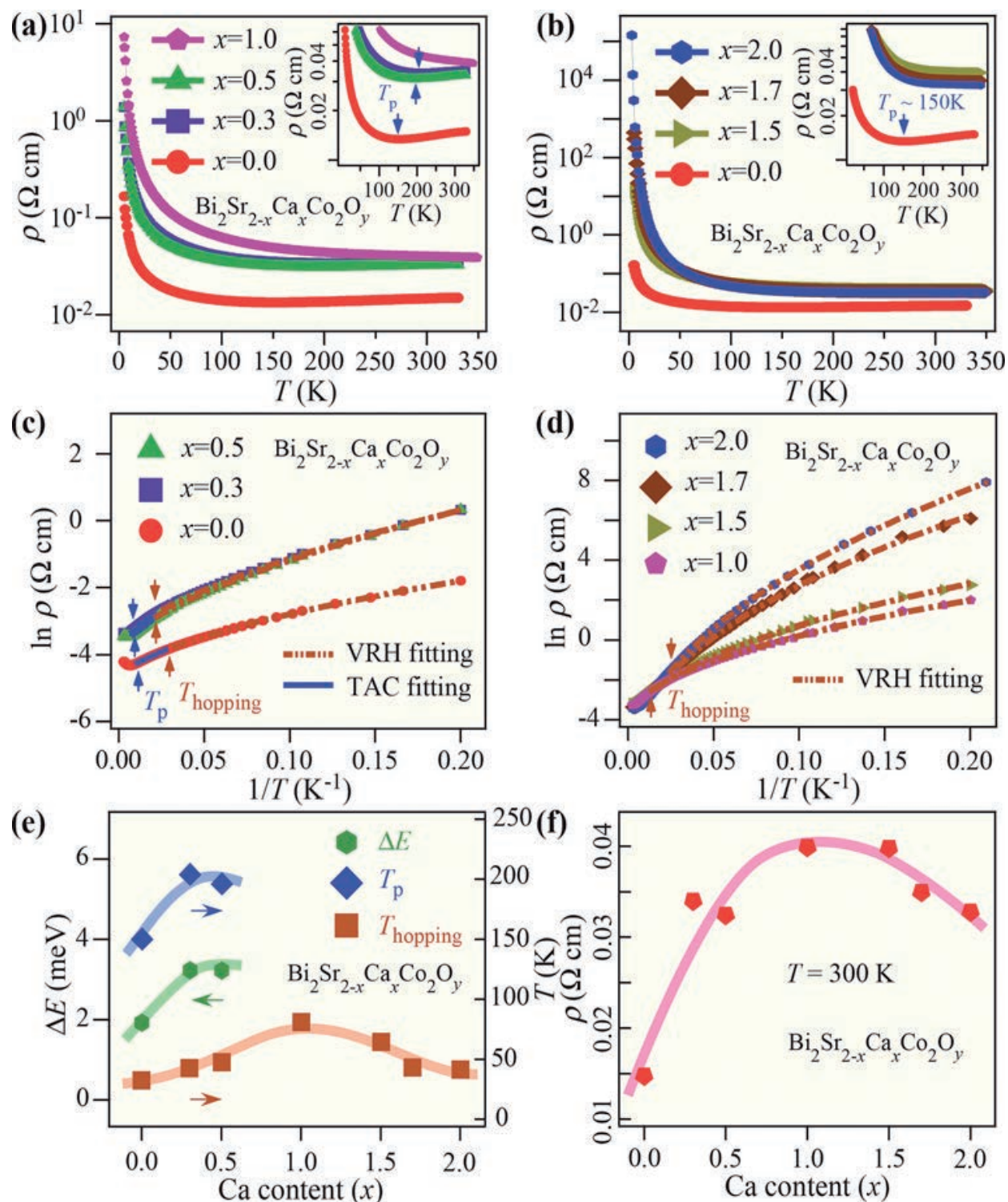
Figure 7. (a) and (b) Temperature dependence of resistivity $\rho(T)$. Insets: magnification plot of $\rho(T)$ for $Bi_2Sr_{2-x}Ca_xCo_2O_y$ samples. (c) and (d) Plot of $\ln\rho$ against $1/T$. Solid lines present TAC fitting. Dashed curves stand for VRH fitting. (e) Ca concentration x dependence of activation energy ΔE, onset temperature T_p of TAC, and onset temperature $T_{hopping}$ of VRH. (f) Ca concentration x dependence of resistivity $\rho_{300\ K}$ at room temperature.

To discern conduction mechanism below T_p, relationship of $\ln\rho$ against $1/T$ is plotted in **Figure 7c** and **d**. As for $x \leq 0.5$, at the beginning, it is found that TAC law matches $\rho(T)$ data well below T_p, namely [35], $\rho(T) = \rho_0 \exp(\Delta E/k_B T)$, where ΔE is activation energy. But $\rho(T)$ apparently deviates from TAC behavior with decreasing the temperature further, and it follows Mott's VRH model described by equation [32]: $\rho(T) = \rho_0 \exp[(T_0/T)^n]$. However, as for $x \geq 1.0$, $\rho(T)$ meets VRH model only, in agreement with the insulating feature of $x = 2.0$ single crystal [1, 42, 43]. Obtained values of ΔE and onset temperature $T_{hopping}$ are plotted in **Figure 7e**. Basically, ΔE increases with Ca content, as well as T_p for $x \leq 0.5$. In comparison, the present value of ΔE based on sintering temperature 800°C is larger than the previous one of $x = 0.0$ at 900°C [8], revealing the difference of grain size effect. It is worth noting that values of $T_{hopping}$ and ρ_{300K} at room temperature first increase and then decrease in whole Ca-doped range (see **Figure 7e** and **f**).

3.2. Enhancement of thermoelectric power driven by Ca doping

Figure 8a shows thermoelectric power $S(T)$ for all samples. Positive values of S demonstrate that majority of charge carriers are hole type. In addition, S exhibits a nearly T-independent behavior above 200 K, while S strongly depends on T peculiarly below 150 K. Ca doping obviously boosts S_{300K} at room temperature especially for heavy Ca contents (see **Figure 8b**). Large S_{300K} value monotonously increases from 105 μV/K($x = 0.0$) to 157 μV/K ($x = 2.0$). In general, the change of S should be related to variation of n. For $x = 0$ single crystal [38], Hall coefficient (R_H) is positive and strongly dependent on the temperature in the range from 300 to 0 K. Increase of R_H toward the lowest temperature is not simple due to the decrease of n, but rather due to anomalous Hall effect. It is noted that variation of R_H with Pb doping is also similar to that of ρ_{ab}. Pb doping slightly reduces the magnitude of R_H, but the increase in number of charge carriers is much smaller than expected from chemical composition [41, 44].

As we know, S is rather low (<10 μV/K) with a metallic behavior in a broad band [7]. Taking into account the tremendous discrepancy, large S of $Bi_2Sr_{2-x}Ca_xCo_2O_y$ with a nearly T-independence at high temperatures in a narrow band should follow the so-called Heikes formula [37]: $S = k_B/e\{\ln[(g_3/g_4)d/(1-d)]\}$, where d is concentration of Co^{4+}, and g_3 and g_4 are spin orbital degeneracies for Co^{3+} and Co^{4+} ions, respectively. Concentration d at room temperature can be deduced from charge carriers' density n. As visible in **Figure 8c**, as for $x< 1.5$, d decreases, while S_{Heikes} (deriving from Heikes formula) increases, which is consistent with the trend of S_{300K}. But for $x \geq 1.5$, reduced S_{Heikes} is reverse to persistent enhancement of S_{300K}. Thus, we have to consider other possible reason of enhanced S for heavily doped samples.

3.3. Specific heat and Sommerfeld coefficient

Next we will check whether the enhanced S originates from the increased effective masses through electronic correlation. To test this point, we performed measurement of specific heat $C(T)$, which is plotted as C/T versus T^2 (see the inset in **Figure 8d**) for selected samples with $x = 0.0, 0.5, 1.5,$ and 2.0. $C(T)$ at low temperatures can be described as $C(T) = \gamma T + \beta T^3$ [45], where γT and βT^3 denote electronic and lattice contribution to $C(T)$, respectively. We can get

electronic coefficient γ by the linear fitting according to $C/T = \gamma + \beta T^2$ [45]. Here, we need to explicitly interpret Sommerfeld coefficient γ. For the present system, unit formula should involve two cobalt atoms. For our polycrystalline sample with $x = 0.0$, a conventional way to get γ by extrapolating high-temperature linear part of C/T versus $T = 0$ gives very large value of ~ 135 mJ mol^{-1} K^{-2} (see **Figure 8d**), comparable with that of $x = 0.0$ single crystal ($\sim$140 mJ mol^{-1} K^{-2}) [41]. However, it is observed that γ rapidly decreases with increasing Ca doping. For our sample with $x = 2.0$, value of γ is $\sim$85 mJ mol^{-1} K^{-2}. Differently, it is noted that value of γ is only 50 mJ mol^{-1} K^{-2} for Bi-Ca-Co-O system, while such a unit formula merely includes one cobalt atom [45].
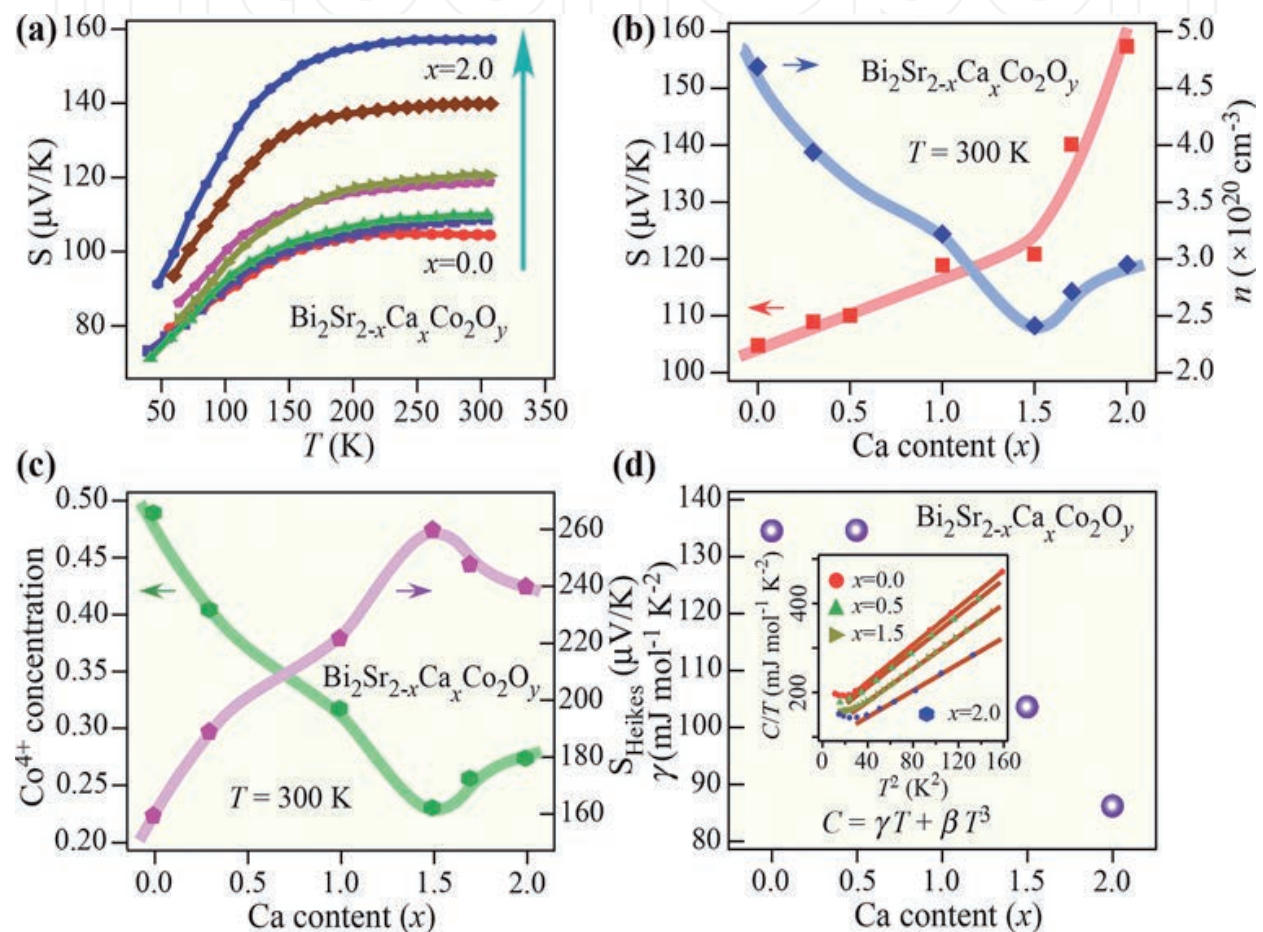
Figure 8. (a) Temperature dependence of thermoelectric power $S(T)$ for Bi$_2$Sr$_{2-x}$Ca$_x$Co$_2$O$_y$ samples. (b) Ca concentration x dependence of S and charge carriers' density n at room temperature, respectively. (c) Ca concentration x dependence of Co^{4+} ion (deduced from charge carriers' density n) and corresponding S_{Heikes} (originating from Heikes formula) at room temperature, respectively. (d) Ca concentration x dependence of electronic coefficient γ deriving from specific heat $C(T)$. Inset: temperature dependence of $C(T)$ plotted as C/T versus T^2 based on fitting lines for $x = 0.0$, 0.5, 1.5, and 2.0, respectively.

Now we discuss the underlying implications of enhanced S with Ca doping. As mentioned above, as for $x < 1.5$, decreased d based on Heikes formula should be responsible for the enhanced S. But for $x \geq 1.5$, local modification of DOS and band structure near E_F could play crucial role. $S(T)$ can be defined by Mott formula [39]: $S(T) = (\pi^2 k_B T)/(3e)[\text{dln}\sigma(E)/\text{d}E]_{E=E_F}$, where $\sigma(E)$ is electrical conductivity with $\sigma(E) = n(E)ev(E)$, $v(E)$ is mobility, $n(E)$ is charge carriers' density with $n(E) = D(E)f(E)$, $D(E)$ is DOS, and $f(E)$ is Fermi function. Apparently, in terms of Mott formula, the enhancement of S for $x \geq 1.5$ should be attributed to the increase of

local DOS near E_F. In details, with decreasing A-site ionic radius (i.e., with increasing Ca content), tolerance factor decreases (not shown here), which leads to changes of lattice distortion in CoO_2 layer and local band structure near E_F, reminiscent of layered perovskite cobaltite $SrLnCoO_4$ (Ln stands for different rare earth elements) [46]. Ultimately, value of S for $x \geq 1.5$ would be enhanced. Based on all of above results, one should emphasize that Sommerfeld coefficient γ is dependent on n, and also as function of DOS at E_F, which leads to continuous enhancement of large S.

4. Thermoelectricity generation and electron-magnon scattering in a natural chalcopyrite mineral

4.1. Crystal structure and SEM characterization

A series of natural chalcopyrite minerals, $Cu_{1+x}Fe_{1-x}S_2$ (x = 0.17, 0.08, and 0.02), were obtained from a hydrothermal vent site named Snow Chimney in the Mariner field of Lau Basin [47]. Basically, mineral composition obtained from intact natural sulfide chimneys has no variation. Subsamples with x = 0.02 and 0.08 were obtained from the most interior chimney part, whereas subsample with x = 0.17 was obtained from the middle chimney wall region. The highly fluctuated and variable physicochemical conditions lead to obvious differences in mineral composition [48]. **Figure 9** shows sketches of its crystal structure and atomic planes, in which chalcopyrite crystallizes in a tetragonal lattice with space group of I-42d and produces honeycomb structure characteristic [49]. Each Fe and Cu atom is encircled by tetrahedron of S atom. The highlighted planes indicateatomic zig-zag pattern, which is likely responsible to phonon scattering. XRD Rietveld refinement of power pattern indicates that three natural samples are single phase with standard chalcopyrite structure. For x = 0.08, refined lattice parameters a and c are 5.278 and 10.402 Å, respectively (see **Figure 10**).
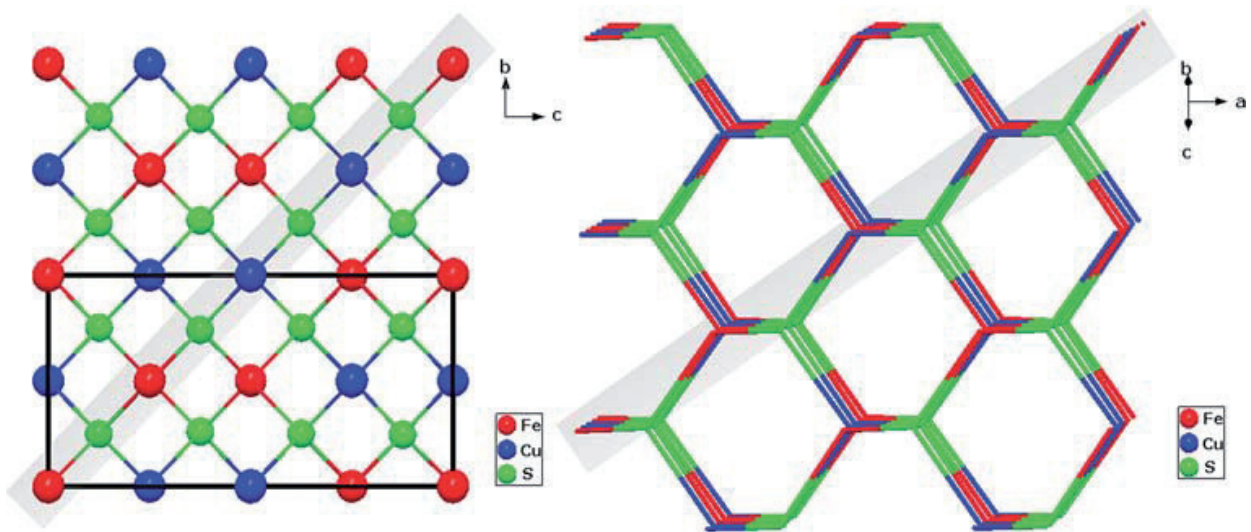

Figure 9. Crystal structure of $Cu_{1+x}Fe_{1-x}S_2$. Ball-and-stick model of the crystal structure (left) viewed along a-axis with black lines indicating unit cell. Stick model (right) showing characteristic honeycomb structure of chalcopyrite. Identical atomic arrangement is highlighted in gray in both structures, but projection is along different axes.
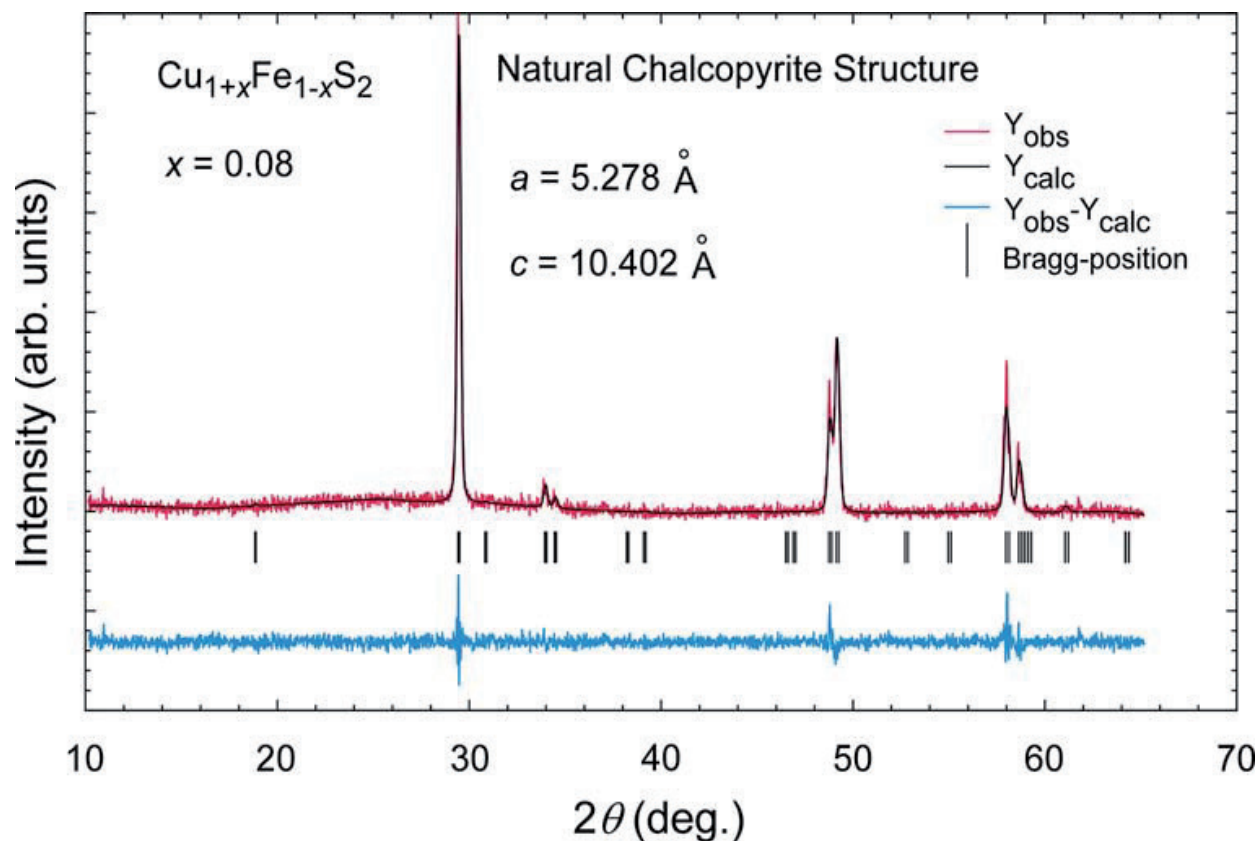
Figure 10. Powder XRD patterns with Rietveld refinement for natural sample of $Cu_{1+x}Fe_{1-x}S_2$ ($x = 0.08$). Red line indicates experimentally observed data, and black line overlapping them refers to calculated data. Vertical tick is related to the Bragg angles positions in space group *I-42d*. The lowest profile shows the difference between observed and calculated patterns. Rietveld refinement indicates that it is standard chalcopyrite structure.

To probe the microstructures of natural $Cu_{1+x}Fe_{1-x}S_2$, we performed SEM characterization (**Figure 11**). SEM analysis revealed that natural chalcopyrite with $x = 0.08$ had layered structure. Three examined natural samples were found to contain morphological diversity, which is characteristic of chalcopyrite minerals, and suggest different physical and chemical behaviors of various microstructures. The SEM observation may provide important insights of the relevance between physical and chemical functions and behaviors of chalcopyrite minerals.
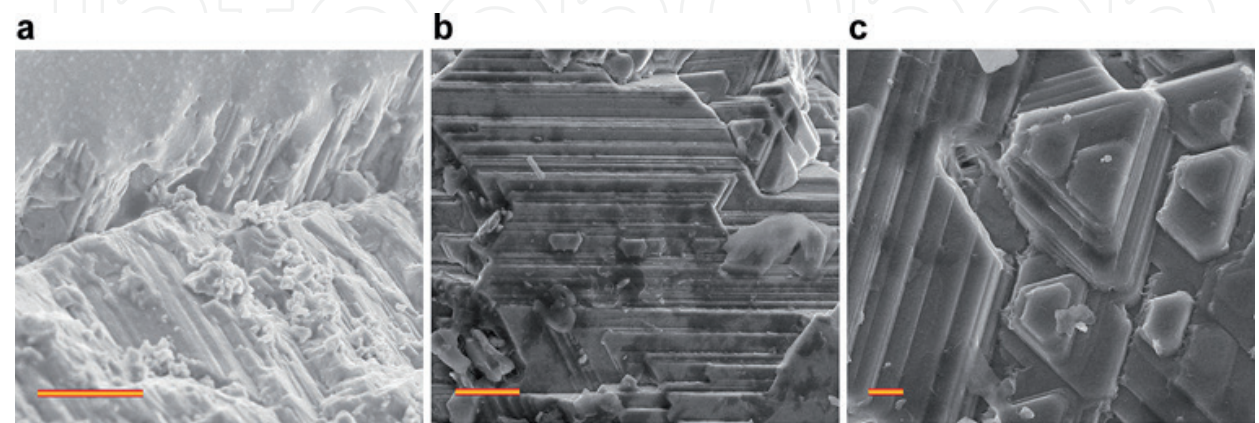

Figure 11. Surface morphology of natural sample of $Cu_{1+x}Fe_{1-x}S_2$ ($x = 0.08$) showing characteristic layered structure. (**a**) Areas showing cracked layered structure in natural sample $Cu_{1+x}Fe_{1-x}S_2$ ($x = 0.08$), scale bar: 10 μm. (**b**) Densely layered structure, scale bar: 5 μm. (**c**) Triangular pattern surrounded by layered structure, scale bar: 1 μm.

4.2. Thermoelectricity generation and electronic states

To examine the functional properties of natural $Cu_{1+x}Fe_{1-x}S_2$ samples, we first measured resistivity (ρ) as function of temperature (T). Three examined natural samples exhibited excellent conductive behavior with semiconductive characteristics (**Figure 12a**). With the reduction of x, the overall resistivity decreased due to the emergence of doped charge carriers. Value of ρ_{300K} for $x = 0.17$, 0.08, and 0.02 was 4.97, 0.11, and 1.01 Ohm×cm, respectively. Compared with $x = 0.08$, the increase of resistivity for $x = 0.02$ stems from the enhanced random Coulomb potential owing to the natural doping.
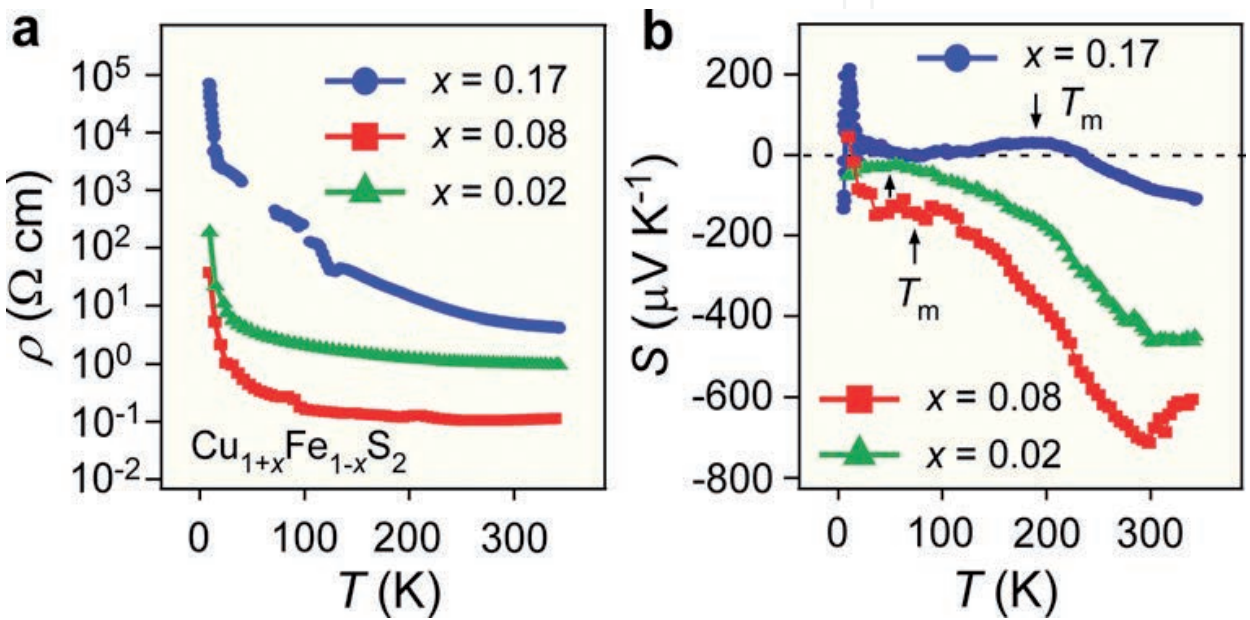
Figure 12. Formation of thermoelectricity by $Cu_{1+x}Fe_{1-x}S_2$. (**a**) Temperature dependence of resistivity ρ in three natural samples of $Cu_{1+x}Fe_{1-x}S_2$. (**b**) Temperature dependence of thermoelectric power S for three samples.

In order to track the evolution of electronic states, we carried out thermoelectric power (S) measurement (**Figure 12b**), where the sign of S changes. For $x = 0.17$, the sign of S switches from negative to positive around 235 K with decreasing temperature (**Figure 12b**). It is amazing to observe two unusual peaks: a broad peak (T_m; 32 µV/K, 186 K) and a sharper peak (T_p; 215 µV/K, 11 K), indicating the majority of hole carriers (p-type). It is of particular interest that, for $x = 0.08$ and 0.02, T_p peak utterly disappears, while T_m peak becomes wider and rapidly shifts to a lower temperature, where S presents very large negative values, demonstrating the majority of electron carriers (n-type), in line with negative Hall coefficient R_H (**Figure 13**). Large S_{300K} reached a remarkable value of −713 and −457 µV/K for $x = 0.08$ and 0.02, respectively. Namely, more electrons are activated at room temperature with increasing Fe concentration. For $x = 0.08$, charge carriers' mobility μ_{300K} and density n_{300K} are 1.8 cm^2 V^{-1} s^{-1} and 3.5 × 10^{19} cm^{-3}, obtained from $R_H = 1/ne$ and $\mu = 1/ne\rho$. In addition, Fe magnetic moment may also play an key role to induce large S, indicative of strong coupling between magnetic ions and doped charge carriers because synthetic $CuFeS_2$ presents AFM ordering at 823 K [15].
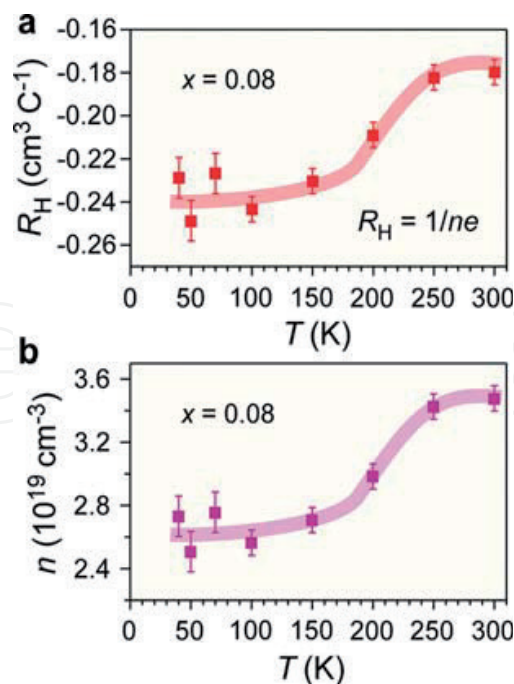
Figure 13. Hall effect of natural sample of $Cu_{1+x}Fe_{1-x}S_2$ ($x = 0.08$). (**a**) Temperature dependence of Hall coefficient R_H. (**b**) Temperature dependence of charge carriers' density n. Value of R_H (cm^3 C^{-1}) is determined by n (cm^{-3}) and electron charge e, that is, $R_H = 1/ne$, where $e = 1.602176 \times 10^{-19}$ C. The shadow in bold is guide to the eyes.

4.3. Electron-magnon scattering and large effective mass

The matter of imperative concern is how to understand the origin of T_m peak and conduction mechanism. According to Mott's formula, S can be qualitatively expressed as $S = -\pi^2 k_B^2 T/3e$ $[\sigma'(E_F)/\sigma(E_F)]$, where k_B is Boltzmann constant, $\sigma(E_F)$ is electrical conductivity at Fermi level E_F, and σ' denotes $d[\sigma(E)]/dE$ [35]. If one assumes σ' is a constant accompanied by isotropic electrical transport properties, namely, $\sigma^{-1} = \rho$, then $\Delta S/S_0$ $\Delta\rho/\rho_0$ can be derived. Plot of $\Delta S/S_0$ versus $\Delta\rho/\rho_0$ for $x = 0.17$ (**Figure 14**) shows that all experimental data near T_m at T_0 from 155 to 300 K deviate from the theoretical calculation, the linearity. These results verify that exotic mechanism of $S(T)$ in natural sample is beyond the framework of conventional thermoelectric picture [50].

To better discern intrinsic transport mechanism of $Cu_{1+x}Fe_{1-x}S_2$, we incorporate spin-wave theory to analyze temperature dependence of S. For $x = 0.08$ and 0.02, field-cooling magnetization and loop hysteresis indicate the localized ferromagnetism (FM) at low temperatures because of additional Fe moments (**Figure 15**). However, strong AFM interaction at high temperatures dominates for three natural samples. Generally speaking, spin waves can scatter electrons for AFM or FM materials, resulting in magnon-drag effect [12]. To check this issue, we developed magnon-drag model, $S = S_0 + S_{3/2}T^{3/2} + S_4T^4$, where S_0 is value of S at $T = 0$, $S_{3/2}T^{3/2}$ term stems from electron-magnon scattering, and S_4T^4 term is related to spin-wave fluctuation in AFM phase. Using this model of magnon drag, the predicted values for three samples closely matched $S(T)$ data (**Figure 16a** and **b**). As the absolute value of $S_{3/2}$ is nearly six orders of magnitude larger than that of S_4 (**Table 1**), electron-magnon scattering dominates $S(T)$ curve. Thus, T_m peak is predicted to originate from magnon drag due to the strong electron-magnon interaction.
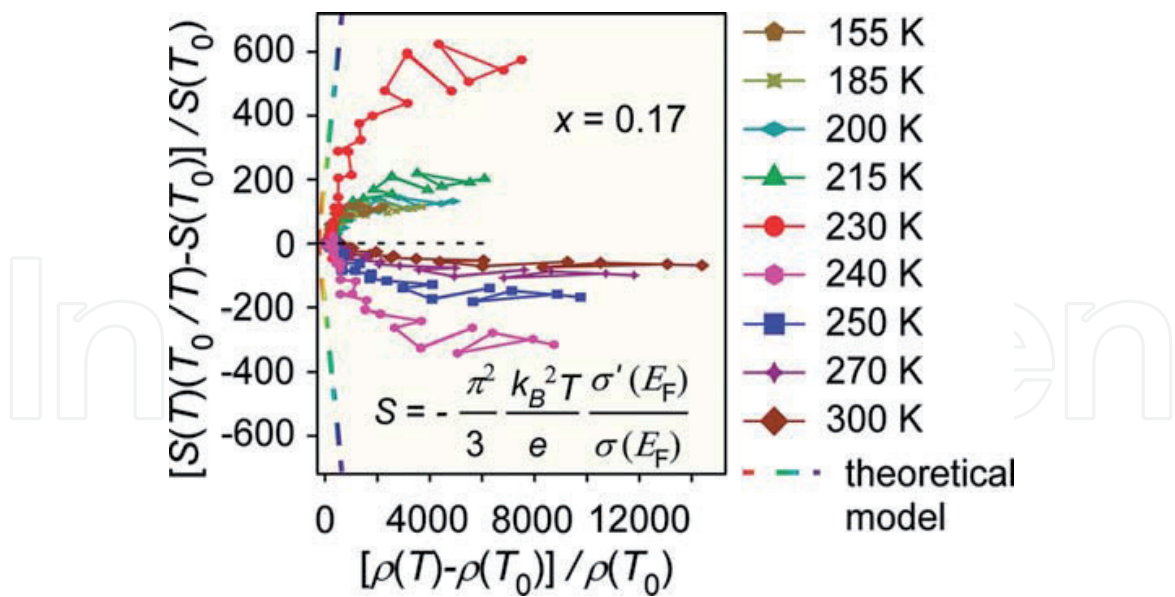
Figure 14. Correlation between thermoelectric power $S(T)$ and resistivity $\rho(T)$. Relative changes of $\Delta S/S_0$ versus $\Delta \rho/\rho_0$ in natural sample with $x = 0.17$ at various temperatures ($T_0 = 155, 185, 200, 215, 230, 240, 250, 270,$ and 300 K). The present experimental data substantially deviates from the linear relationship predicted by Mott's formula, which is indicated by dotted line.
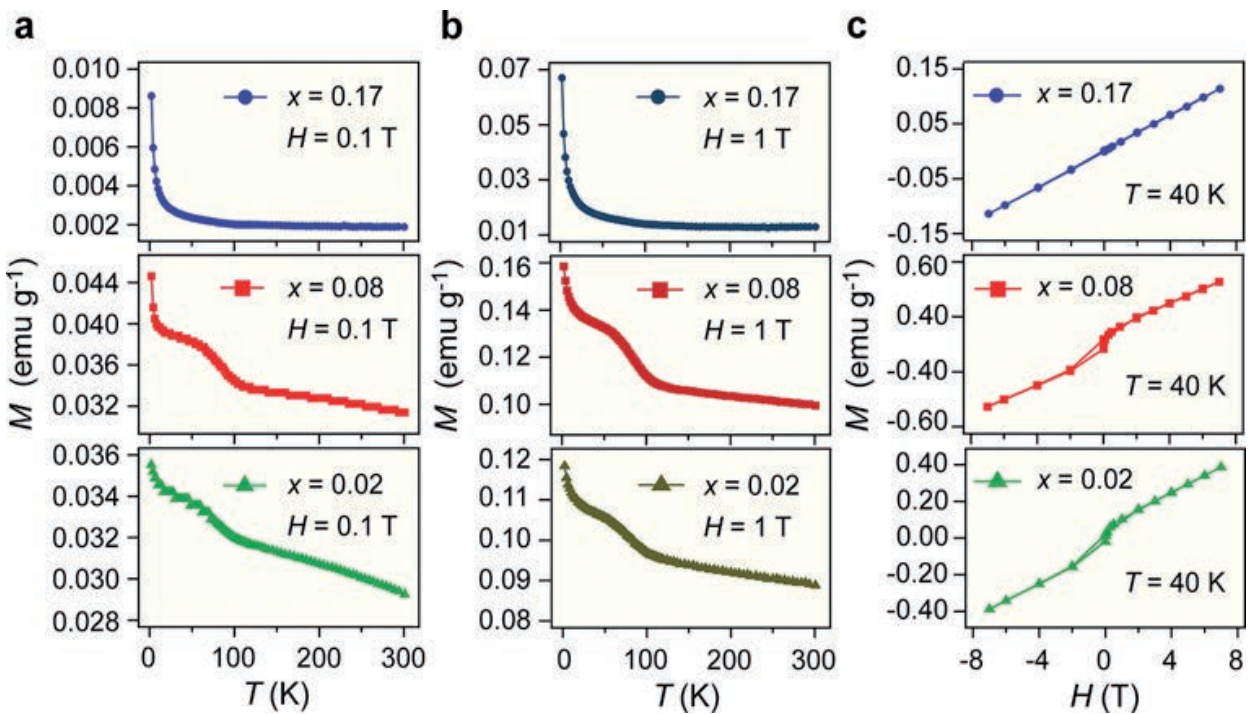

Figure 15. Magnetic properties of natural $Cu_{1+x}Fe_{1-x}S_2$. (**a**, **b**) Temperature dependence of field-cooling (FC) magnetization, M, in three natural samples of $Cu_{1+x}Fe_{1-x}S_2$, measured in applied magnetic field of $H = 0.1$ T (**a**) and $H = 1$ T (**b**). (**c**) Magnetic field dependence of magnetization, M, for three samples, measured at 40 K.

To gain more insight into the correlation between magnon drag, doped carriers, and S, we plotted parameters S_0, $S_{3/2}$, and S_4 as a function of x (**Table 1**). S_0, $S_{3/2}$, and S_4 for $x = 0.08$ has largest absolute values among three natural samples, in agreement with the largest S, smallest ρ, and highest power factor. Unlike S_0 and S_4, dependence of $S_{3/2}$ is quite unique (**Figure 16c**). The sign of $S_{3/2}$ varies from positive to negative with increasing Fe concentration, suggesting

the alternation of p-type and n-type charge carriers and orbital degree of freedom of Fe $3d$ band with AFM ordering. Additionally, electron-magnon scattering occupies thermoelectric properties, indicating strong coupling between doped charge carriers and AFM spins. Furthermore, $\rho(T)$ follows TAC model $\rho(T) = \rho_0 \exp(\Delta E / k_B T)$, where ΔE is activation energy [35]. Notably, the fitted energy gap of ΔE (60.1, 4.9, and 11.8 meV for $x = 0.17$, 0.08, and 0.02, respectively), which verifies the existence of localized Fe spins, is markedly smaller than that of artificial chalcopyrite [21, 29–31]. It is noted that experimental $S(T)$ result is well described by electron-magnon scattering up to ~200 K, while it deviates from theoretical lines for higher temperatures. In particular, power factor S^2/ρ shows an abrupt enhancement above 200 K for $x = 0.08$ (**Figure 16d**), in agreement with that of R_H and n (**Figure 13**). Above 200 K, large effective mass (m^*) leads to high power factor and large S due to low μ and high n. For $x = 0.08$, it exhibits the largest m^* value (1.6 m_0) at room temperature, where m_0 is free electron mass. Therefore, we can conclude that robust electron-magnon scattering and large m^* induce unexpected thermoelectricity generation in natural chalcopyrite mineral.
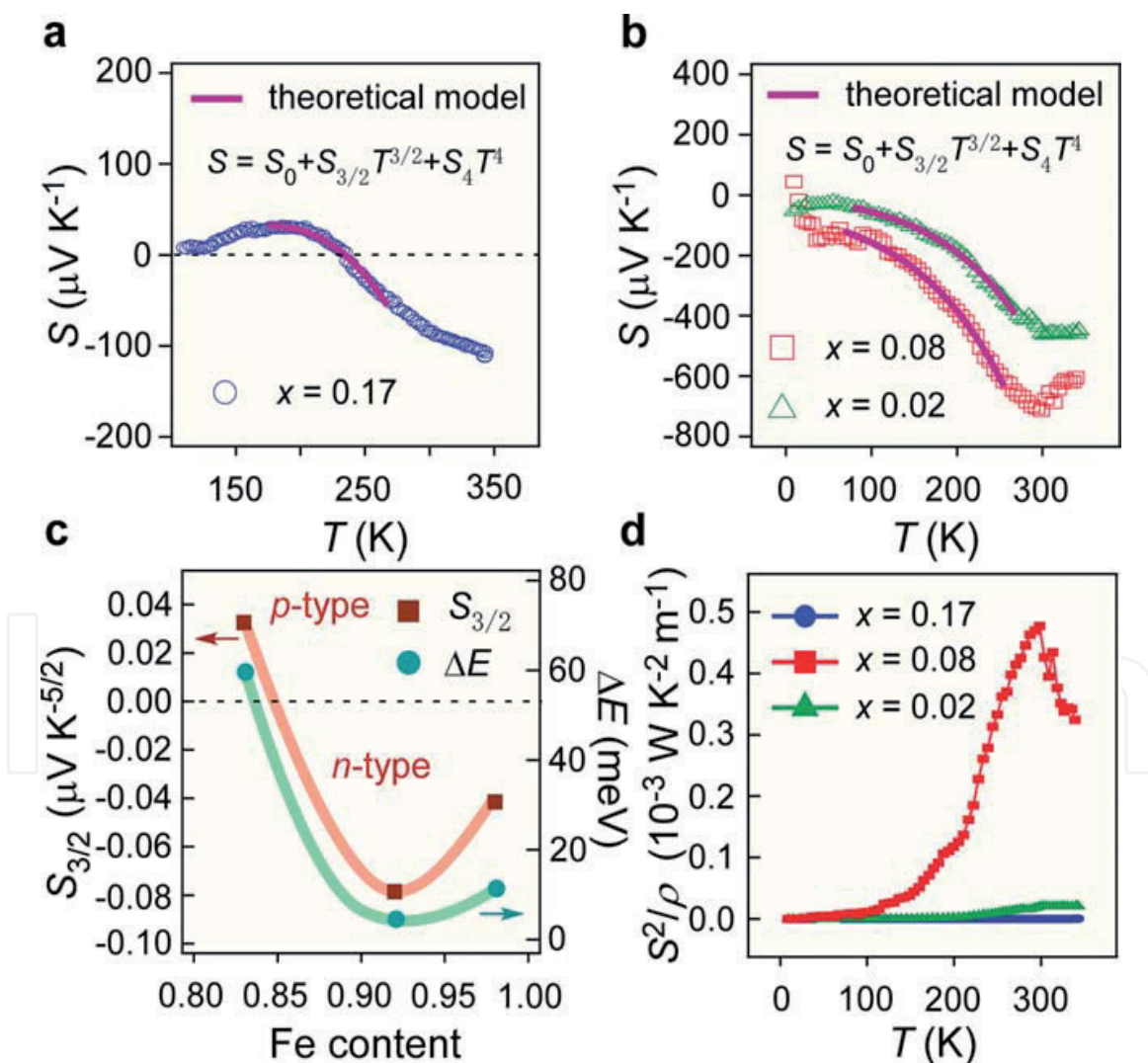
Figure 16. Temperature dependence of S for $Cu_{1+x}Fe_{1-x}S_2$ samples with $x = 0.17$ (**a**) and $x = 0.08$ and 0.02 (**b**). Symbols represent experimental data and solid lines correspond to theoretical simulation based on the model of magnon drag, $S = S_0 + S_{3/2}T^{3/2} + S_4T^4$. (**c**) Obtained parameters $S_{3/2}$ and ΔE are plotted as function of Fe content, where $S_{3/2}$ represents the electron-magnon scattering process and ΔE is activation energy. (**d**) Temperature dependence of power factor, S^2/ρ, for three samples.

Parameter	T_m(K)	S_0(μVK^{-1})	$S_{3/2}$(μVK$^{-5/2}$)	S_4 (μVK^{-5})	ΔE(meV)
x = 0.17	186	−6.21	0.03	−3.84×10^{-8}	60.1
x = 0.08	68	−75.45	−0.08	−5.47×10^{-8}	4.9
x = 0.02	38	−10.61	−0.04	−3.95×10^{-8}	11.8

The parameter T_m represents the peak of magnon drag, which stems from the experimental $S(T)$ curve. The parameters S_0, $S_{3/2}$, and S_4 stem from the model of magnon drag, $S = S_0 + S_{3/2}T^{3/2} + S_4T^4$. The parameter ΔE is the activation energy, which stems from the TAC model, $\rho(T) = \rho_0 \exp(\Delta E/k_B T)$.

Table 1. Obtained parameters based on theoretical simulation.

In terms of thermal conductivity κ, phononic component κ_{ph} dominates for three natural samples owing to negligible electronic component κ_e (**Figure 17**). For the optimal sample with x = 0.08, value of ZT can reach 0.03 at room temperature (**Figure 17**), thus indicating that natural chalcopyrite semiconductor is a promising candidate for thermoelectric energy materials. It is quite striking that the spontaneous doping process during deep-sea hydrothermal vent mineral precipitations led to natural thermoelectric improvement, which is similar to natural mineral tetrahedrites [51].
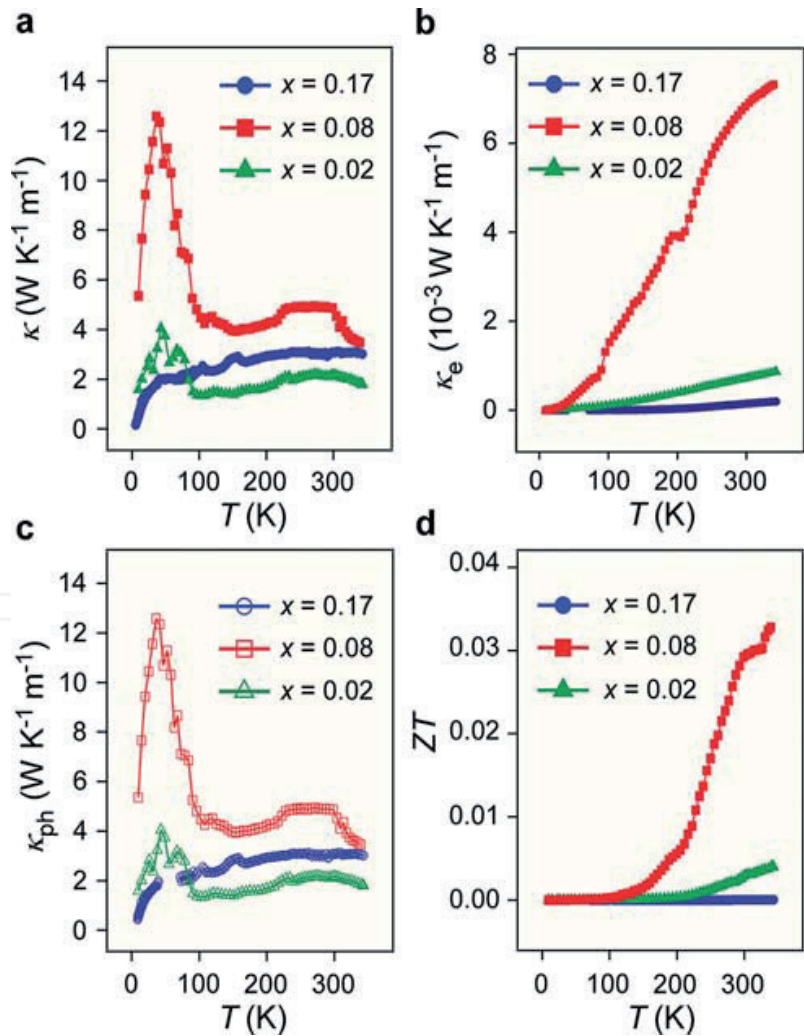

Figure 17. Thermal conductivity and phonon scattering of natural Cu$_{1+x}$Fe$_{1-x}$S$_2$. (**a**) Temperature dependence of total thermal conductivity κ. (**b**) Temperature dependence of electronic component κ_e. (**c**) Temperature dependence of phononic component κ_{ph}. (**d**) Temperature dependence of dimensionless figure of merit ZT.

5. Conclusions

Our results of layered cobaltites $Bi_2Sr_2Co_2O_y$ system based on narrow band model are not only helpful to understand large S and transport mechanism but also differentiate other systems based on a broad band model. In particular, we give the experimental evidence by Hall effect and $C(T)$ measurements, demonstrating that Sommerfeld coefficient γ is dependent on charge carriers' density n, and also as a function of DOS at E_F, which induces exotic enhancement of large S in $Bi_2Sr_{2-x}Ca_xCo_2O_y$. Especially for $Bi_2Sr_{1.9}Ca_{0.1}Co_2O_y$, it may provide an excellent platform to be regarded as potential candidates for thermoelectric materials.

In addition, we demonstrated direct thermoelectricity generation in natural chalcogenides, $Cu_{1+x}Fe_{1-x}S_2$, which was shown to have large S value and high power factor in the low x region, in which electron-magnon scattering and large m^* values were detected. Since doped charge carriers exist in strong coupling with localized spins, the unusual alternation of p- and n-type carriers should be of paramount importance in understanding charge dynamics arising from $3d$ orbital degrees of freedom. Such a finding of exotic thermoelectric properties in natural but not synthetic chalcopyrite opens a novel research field for manipulating low-cost thermoelectricity or even electron/hole carriers, providing therefore a new perspective on technical feasibility for designing and pinpointing the surface-morphology-engineered devices via the naturally abundant materials.

Acknowledgements

Author details

Ran Ang

Address all correspondence to: rang@scu.edu.cn

1 Key Laboratory of Radiation Physics and Technology, Ministry of Education, Institute of Nuclear Science and Technology, Sichuan University, Chengdu, China

2 Institute of New Energy and Low-Carbon Technology, Sichuan University, Chengdu, China

References

[1] Tarascon J M, Ramesh R, Barboux P, Hedge M S, Hull G W, Greene L H, et al.: New non-superconducting layered Bi-oxide phases of formula $Bi_2M_3Co_2O_y$ containing Co instead of Cu. Solid State Communications. 1989;**71**:663–668. DOI: 10.1016/0038-1098(89)91813-9

[2] Funahashi R, Matsubara I, Sodeoka S.: Thermoelectric properties of $Bi_2Sr_2Co_2O_x$ poly-crystalline materials. Applied Physics Letters. 2000;**76**:2385–2387. DOI: 10.1063/1.126354

[3] Koumoto K, Terasaki I, Funahashi R.:Complex oxide materials for potential thermoelectric applications. MRS Bulletin. 2006;**31**:206–210. DOI: 10.1557/mrs2006.46

[4] Terasaki I, Sasago Y, Uchinokura K.: Large thermoelectric power in $NaCo_2O_4$ single crystals. Physical Review B. 1997;**56**:R12685–12687. DOI: 10.1103/PhysRevB.56.R12685

[5] Masset A C, Michel C, Maignan A, Hervieu M, Toulemonde O, Studer F, et al.: Misfit-layered cobaltite with an anisotropic giant magnetoresistance: $Ca_3Co_4O_9$. Physical Review B. 2000;**62**:166–175. DOI: 10.1103/PhysRevB.62.166

[6] Itoh T, Terasaki I.: Thermoelectric Properties of $Bi_{2.3-x}Pb_xSr_{2.6}Co_2O_y$ single crystals. Japanese Journal of Applied Physics. 2000;**39**:6658–6660. DOI: 10.1143/JJAP.39.6658

[7] Heikes R R, Ure R W.: Thermoelectricity: Science and Engineering. New York: Interscience; 1961. 576 p.

[8] Yin L H, Ang R, Huang Y N, Jiang H B, Zhao B C, Zhu X B, et al.: The contribution of narrow band and modulation of thermoelectric performance in doped layered cobaltites $Bi_2Sr_2Co_2O_y$. Applied Physics Letters. 2012;**100**:173503. DOI: 10.1063/1.4705429

[9] Yin L H, Ang R, Huang Z H, Liu Y, Tan S G, Huang Y N, et al.: Exotic reinforcement of thermoelectric power driven by Ca doping in layered $Bi_2Sr_{2-x}Ca_xCo_2O_y$. Applied Physics Letters. 2013;**102**:141907. DOI: 10.1063/1.4801644

[10] Sootsman J R, Chung D Y, Kanatzidis M G.: New and old concepts in thermoelectric materials. Angewandte Chemie International Edition. 2009;**48**:8616–8639. DOI: 10.1002/anie.200900598

[11] Chen Y L, Liu Z K, Analytis J G, Chu J H, Zhang H J, Yan B H, et al.: Single Dirac cone topological surface state and unusual thermoelectric property of compounds from a new topological insulator family. Physical Review Letters. 2010;**105**:266401. DOI: 10.1103/PhysRevLett.105.266401

[12] Costache MV, Bridoux G, Neumann I, Valenzuela SO.: Magnon-drag thermopile. Nature Materials. 2011;**11**:199–202. DOI: 10.1038/nmat3201

[13] Ekwo P I, Okeke C E.: Thermoelectric properties of the PbS ZnS alloy semiconductor and its application to solar energy conversion. Energy Conversion and Management. 1992;**33**:159–164. DOI: 10.1016/0196-8904(92)90121-C

[14] Donnay G, Corliss L M, Donnay J D H, Elliott N, Hastings J M.: Symmetry of magnetic structures: Magnetic structure of chalcopyrite. Physical Review. 1958;**112**:1917–1923. DOI: 10.1103/PhysRev.112.1917

[15] Teranishi T.: Magnetic and electric properties of chalcopyrite. Journal of the Physical Society of Japan. 1961;**16**:1881–1887. DOI: 10.1143/JPSJ.16.1881

[16] Tossell J A, Urch D S, Vaughan D J, Wiech G.: The electronic structure of $CuFeS_2$, chalcopyrite, from x-ray emission and x-ray photoelectron spectroscopy and $X\alpha$ calculations. The Journal of Chemical Physics. 1982;**77**:77–82. DOI: 10.1063/1.443603

[17] Fujisawa M, Suga S, Mizokawa T, Fujimori A, Sato K.: Electronic structures of $CuFeS_2$ and $CuAl_{0.9}Fe_{0.1}S_2$ studied by electron and optical spectroscopies. Physical Review B. 1994;**49**:7155–7164. DOI: 10.1103/PhysRevB.49.7155

[18] Nakamura R, Takashima T, Kato S, Takai K, Yamamoto M, Hashimoto K.: Electrical current generation across a Black Smoker Chimney. Angewandte Chemie International Edition. 2010;**49**:7692–7694. DOI: 10.1002/anie.201003311

[19] Lovesey S W, Knight K S, Detlefs C, Huang S W, Scagnoli V, Staub U.: Acentric magnetic and optical properties of chalcopyrite ($CuFeS_2$). Journal of Physics: Condensed Matter. 2012;**24**:216001. DOI: 10.1088/0953-8984/24/21/216001

[20] Lyubutin I S, Lin C R, Starchikov S S, Siao Y J, Shaikh M O, Funtov K O, et al.: Synthesis, structural and magnetic properties of self-organized single-crystalline nanobricks of chalcopyrite $CuFeS_2$. Acta Materialia. 2013;**61**:3956–3962. DOI: 10.1016/j.actamat.2013.03.009

[21] Tsujii N, Mori T.: High thermoelectric power factor in a carrier-doped magnetic semiconductor $CuFeS_2$. Applied Physics Express. 2013;**6**:043001. DOI: 10.7567/APEX.6.043001

[22] Goodman C H L, Douglas R W.: New semiconducting compounds of diamond type structure. Physica. 1954;**20**:1107–1109. DOI: 10.1016/S0031-8914(54)80247-3

[23] Austin I G, Goodman C H L, Pengelly A E.: New semiconductors with the chalcopyrite structure. Journal of The Electrochemical Society. 1956;**103**:609–610. DOI: 10.1149/1.2430171

[24] Nikiforov K G.: Magnetically ordered multinary semiconductors. Progress in Crystal Growth and Characterization of Materials. 1999;**39**:1–104. DOI: 10.1016/S0960-8974(99)00016-9

[25] Koschel W H, Sorger F, Baars J.: Optical phonons in I-III-VI$_2$ compounds. Le Journal De Physique Colloques. 1975;**36**:C3:177–181. DOI: http://dx.doi.org/10.1051/jphyscol:1975332

[26] Koschel W H, Bettini M.: Zone-centered phonons in $A^IB^{III}S_2$ chalcopyrites. Physica Status Solidi B. 1975;**72**:729–737. DOI: 10.1002/pssb.2220720233

[27] Sato K, Harada Y, Taguchi M, Shin S, Fujimori A.: Characterization of Fe 3d states in $CuFeS_2$ by resonant X-ray emission spectroscopy. Physica Status Solidi A. 2009;**206**:1096–1100. DOI: 10.1002/pssa.200881196

[28] Woolley J C, Lamarche A M, Lamarche G, Quintero M, Swainson I P, Holden T M.: Low temperature magnetic behaviour of $CuFeS_2$ from neutron diffraction data. Journal of Magnetism and Magnetic Materials. 1996;**162**:347–354. DOI: 10.1016/S0304-8853(96)00252-1

[29] Austin I G, Goodman C H L, Pengelly A E.: Semiconductors with chalcopyrite structure. Nature. 1956;**178**:433. DOI: 10.1038/178433a0

[30] Hamajima T, Kambara T, Gondaira K I, Oguchi T.: Self-consistent electronic structures of magnetic semiconductors by a discrete variational Xα calculation. III. Chalcopyrite $CuFeS_2$. Physical Review B. 1981;**24**:3349–3353. DOI: 10.1103/PhysRevB.24.3349

[31] Teranishi T, Sato K, Kondo K.:Optical properties of a magnetic semiconductor: Chalcopy-rite $CuFeS_2$.: I. Absorption spectra of $CuFeS_2$ and Fe-Doped $CuAlS_2$ and $CuGaS_2$. Journal of the Physical Society of Japan. 1974;**36**:1618–1624. DOI: 10.1143/JPSJ.36.1618

[32] Tsujii N, Mori T, Isoda Y.: Phase stability and thermoelectric properties of $CuFeS_2$-based magnetic semiconductor. Journal of Electronic Materials. 2014;**43**:2371–2375. DOI: 10.1007/s11664-014-3072-y

[33] Ang R, Khan A U, Tsujii N, Takai K, Nakamura R, Mori T.: Thermoelectricity generation and electron-magnon scattering in a natural chalcopyrite mineral from a deep-sea hydro-thermal vent. Angewandte Chemie International Edition. 2015;**54**:12909–12913. DOI: 10.1002/anie.201505517

[34] Yamamoto T, Tsukada I, Uchinokura K, Takagi M, Tsubone T, Ichihara M, et al.: Structural phase transition and metallic behavior in misfit layered (Bi,Pb)-Sr-Co-O System. Japanese Journal of Applied Physics. 2000;**39**:L747–750. DOI: 10.1143/JJAP.39.L747

[35] Mott N F, Davis E A.: Electronic Processes in Non-Crystalline Materials. Oxford: Clarendon; 1971. 437 p.

[36] Zvyagin I P.: On the theory of hopping transport in disordered semiconductors. Physica Status Solidi B. 1973;**58**:443–449. DOI: 10.1002/pssb.2220580203

[37] Kittel C.: Introduction to Solid State Physics. Singapore: Wiley; 2001.

[38] MacDonald D K C.: Thermoelectricity: An Introduction to the Principles. New York: Wiley; 1962. 133 p.

[39] Takeuchi T, Kondo T, Takami T, Takahashi H, Ikuta H, Mizutani U, et al.: Contribution of electronic structure to the large thermoelectric power in layered cobalt oxides. Physical Review B. 2004;**69**:125410. DOI: 10.1103/PhysRevB.69.125410

[40] Asahi R, Sugiyama J, Tani T.: Electronic structure of misfit-layered calcium cobaltite. Physical Review B. 2002;**66**:155103. DOI: 10.1103/PhysRevB.66.155103

[41] Yamamoto T, Uchinokura K, Tsukada I.: Physical properties of the misfit-layered (Bi,Pb)-Sr-Co-O system: Effect of hole doping into a triangular lattice formed by low-spin Co ions. Physical Review B. 2002;**65**:184434. DOI: 10.1103/PhysRevB.65.184434

[42] Watanabe Y, Tsui D C, Birmingham J T, Ong N P, Tarascon J M.: Infrared reflectivity of single-crystal $Bi_2M_{m+1}Co_mO_y$ (M=Ca,Sr,Ba; m=1,2), $Bi_2Sr_3Fe_2O_{9.2}$, and $Bi_2Sr_2MnO_{6.25}$, isomorphic to Bi-Cu-based high-Tc oxides. Physical Review B. 1991;**43**:3026–3033. DOI: 10.1103/PhysRevB.43.3026

[43] Terasaki I, Nakahashi T, Maeda A, Uchinokura K.: Optical reflectivity of single-crystal $Bi_2M_3Co_2O_{9+\delta}$ (M=Ca, Sr, and Ba) from the infrared to the vacuum-ultraviolet region. Physical Review B. 1993;**47**:451–456. DOI: 10.1103/PhysRevB.47.451

[44] Yamamoto T, Tsukada I, Takagi M, Tsubone T, Uchinokura K.: Hall effect in a layered magnetoresistive cobalt oxide. Journal of Magnetism and Magnetic Materials. 2001;**226–230**:2031–2032. DOI: 10.1016/S0304-8853(00)00670-3

[45] Limelette P, Hbert S, Hardy V, Frsard R, Simon Ch, Maignan A.: Scaling Behavior in thermoelectric misfit cobalt oxides. Physical Review Letters. 2006;**97**:046601. DOI: 10.1103/PhysRevLett.97.046601

[46] Ang R, Sun Y P, Luo X, Hao C Y, Song W H.: Studies of structural, magnetic, electrical and thermal properties in layered perovskite cobaltite $SrLnCoO_4$ (Ln = La, Ce, Pr, Nd, Eu, Gd and Tb). Journal of Physics D: Applied Physics. 2008;**41**:045404. DOI: 10.1088/0022-3727/41/4/045404

[47] Takai K, Nunoura T, Ishibashi J, Lupton J, Suzuki R, et al. Variability in the microbial communities and hydrothermal fluid chemistry at the newly discovered Mariner hydrothermal field, southern Lau Basin. Journal of Geophysical Research. 2008;**113**:G02031. DOI: 10.1029/2007JG000636

[48] Tivey M K. The influence of hydrothermal fluid composition and advection rates on black smoker chimney mineralogy: Insights from modeling transport and reaction. Geochimica et Cosmochimica Acta. 1995;**59**:1933–1949. DOI: 10.1016/0016-7037(95)00118-2

[49] Goodman C H L. A new group of compounds with diamond type (chalcopyrite) structure. Nature. 1957;**179**:828–829. DOI: 10.1038/179828b0

[50] Asamitsu A, Moritomo Y, Tokura Y. Thermoelectric effect in $La_{1-x}Sr_xMnO_3$. Physical Review B. 1996;**53**:R2952–2955. DOI: 10.1103/PhysRevB.53.R2952

[51] Lu X, Morelli D T, Xia Y, Zhou F, Ozolins V, Chi H, et al. High performance thermoelectricity in earth-abundant compounds based on natural mineral tetrahedrites. Advanced Energy Materials. 2013;**3**:342–348. DOI: 10.1002/aenm.201200650